Spatial Discretization of the Shallow Water Equations in Spherical Geometry Using Osher's Scheme

D. Lanser, J. G. Blom, and J. G. Verwer

CWI, P.O. Box 94079, 1090 GB Amsterdam, The Netherlands
E-mail: debby.lanser@cwi.nl, joke.blom@cwi.nl, jan.verwer@cwi.nl

The shallow water equations in spherical geometry provide a first prototype for developing and testing numerical algorithms for atmospheric circulation models. Since the seventies these models have often been solved with spectral methods. Increasing demands on grid resolution combined with massive parallelism and local grid refinement seem to offer significantly better perspectives for gridpoint methods. In this paper we study the use of Osher's finite-volume scheme for the spatial discretization of the shallow water equations on the rotating sphere. This finite volume scheme of upwind type is well suited for solving a hyperbolic system of equations. Special attention is paid to the pole problem. To that end Osher's scheme is applied on the common (reduced) latitude-longitude grid and on a stereographic grid. The latter is most appropriate in the polar region as in stereographic coordinates the pole singularity does not exist. The latitude-longitude grid is preferred on lower latitudes. Therefore, across the sphere we apply Osher's scheme on a combined grid connecting the two grids at high latitude. We will show that this provides an attractive spatial discretization for explicit integration methods, as it can greatly reduce the time step limitation incurred by the pole singularity when using a latitude-longitude grid only. When time step limitation plays no significant role, the standard (reduced) latitude-longitude grid is advocated provided that the grid is kept sufficiently fine in the polar region to resolve flow over the poles. ⓒ 2000 Academic Press

Key Words: numerical solution of PDEs; atmospheric flow; SWEs in spherical geometry; Osher's scheme; stereographic coordinates.

1. INTRODUCTION

People have long tried to forecast the weather, first by observation of current and historical meteorological data and later by numerical simulation with circulation models based on atmospheric primitive equations [4, 7, 10, 12]. Today, circulation models are widespread.

In addition to being used in weather forecasting, they are applied as climate simulation models and provide meteorological input data needed in air pollution descriptions.

During the sixties the field of frequently used approximation methods in circulation models consisted mainly of gridpoint methods. When Orszag and Eliasen *et al.* [6, 13] introduced the spectral transform method in global atmospheric modeling, this accent shifted. Because spectral methods proved to be very accurate and cost efficient, they started to dominate the field of approximation methods used in global atmospheric modeling. Recently the discussion on numerical methods applicable in circulation models has been renewed. Spectral methods are no longer considered ideal. Progression in atmospheric modeling, on the meteorological as well as on the computational side, demands higher grid resolutions than in the past. The workload of a spectral method grows very fast when the number of gridpoints is increased. Therefore, the relevant question can be posed whether at high resolutions an improved gridpoint method can compete with a spectral method. This is also stated in [3, 5]. In addition, the global property of a spectral method has some other drawbacks. Although this property contributes highly to the accuracy of the found solution, it leads to inconveniences when one tries to parallelize spectral codes on parallel machines with distributed memory. Furthermore, a spectral method can suffer from Gibb's phenomena (spectral ringing) when applied in areas where flow patterns with strong gradients are encountered, for example, in front simulation.

In this paper we develop a new numerical gridpoint method. We apply a finite volume method of upwind type. We decided on this method, because it is conservative and respects the characteristic directions associated with the hyperbolic character of our equations. In addition, compared to a spectral method, it behaves well in areas where flow patterns with strong gradients are expected. From the class of finite volume methods, Osher's approximate Riemann solver makes a good choice. First, it is robust and second-order accurate when combined with the right state interpolation. Second, from a future perspective, it has a logical extension to more realistic primitive equations and it has a consistent boundary treatment, which makes Osher's solver preferable to, for instance, Roe's solver. Finally, our upwind scheme is a scheme of flux difference splitting type (FDS). Schemes of flux vector splitting type (FVS) do not provide an alternative in this case, since the necessary condition for these schemes, i.e., that the Jacobian of the flux vector is homogeneous of degree 1, is not fulfilled. For a detailed description of FDS and FVS methods we refer to [9].

To avoid the well-known pole problem [20], which arises when a gridpoint method is applied on a full uniform latitude–longitude grid, we study a reduced lat–lon grid and a combined grid composed of a (reduced) lat–lon grid away from the poles and a stereographic grid at the two polar caps. The combined grid consists of three computational domains with a rectangular grid almost everywhere. All three mappings used to map the physical domain onto the computational domain are conformal. These qualities yield flux calculations that are simple and straightforward. The use of a stereographic grid has been proposed before by Phillips [16] and Browning *et al.* [2].

To validate our discretization scheme and grid, we consider the 2D shallow water equations (SWEs) on the rotating sphere, which serve as a first prototype for a circulation model. The SWEs describe the behavior of a shallow homogeneous incompressible and inviscid fluid layer. Although in comparison to the full set of atmospheric primitive equations, the SWEs are incomplete, they present some of the major difficulties associated with the horizontal dynamical aspects of circulation models on the earth.

In Section 2 we focus on the formulation of the SWEs in the two different coordinate systems. In Section 3.1 we attend to the construction of our combined grid. The spatial discretization of the equations, i.e., a description of our finite volume method, is given in Section 3.2. Special attention is paid to the connection problem, which occurs at the grid interface, when coupling the spherical grid part with the stereocaps. Numerical results from calculations on combined grids and on fully lat–lon grids are given in Section 4. Calculations are done on test case 2 of the test set in [27], which is standard for testing new numerical methods for solving the SWEs in spherical geometry. Test case 2 provides us with a good nonlinear test to evaluate the scheme's ability to handle the poles. Since the test set consists of problems with smooth flow patterns, it does not provide a test to reveal all favorable features of our scheme. Therefore, the objective of this paper can best be summarized as a first validation of whether the Osher scheme applied on a combined grid yields an appropriate candidate to solve the SWEs in spherical geometry. The main conclusions of our investigations are formulated in Section 5.

2. THE SHALLOW WATER EQUATIONS

Since they cover important aspects of the horizontal dynamical behavior of the atmosphere, the SWEs on the sphere suffice as a first prototype of a circulation model. Through the laws of conservation of mass and momentum, the SWEs on the sphere can be derived to describe the behavior (velocities and fluid depth) of a shallow homogeneous incompressible and inviscid fluid layer on the earth. In other words, we assume that the atmosphere can be regarded as a thin layer of air in which the density is uniform and constant, and viscous effects can be ignored. By using the SWEs, it is further assumed that the velocity component normal to the earth surface, the vertical component, can be neglected compared to the horizontal velocity component. Furthermore, the vertical component of the Coriolis acceleration is neglected in comparison with gravity. The acceleration of gravity, g, is assumed to be constant, containing both the effects related to the centrifugal force and the gravitational attraction of the earth. The pressure gradient force is considered to be hydrostatic. The SWEs then follow from the Navier Stokes equations on the rotating sphere by integration over the fluid depth (depth-averaging); for details see [7]. A derivation of more realistic atmospheric primitive equations can be found in [7, 10].

2.1. The Shallow Water Equations in Spherical Coordinates

Let (λ, ϕ, t) denote the independent variables longitude ($\lambda \in [0, 2\pi)$), latitude ($\phi \in [-\frac{\pi}{2}, +\frac{\pi}{2}]$), and time ($t \geq 0$). Let u be the velocity in the longitudinal direction, v the velocity in the latitudinal direction, and H the depth of the fluid layer. Let h be the height of the free surface above the sphere at sea level, $h = H + h_s$, where h_s accounts for the orography of the earth associated with the height of mountains. Further, let $\underline{u}$ denote the horizontal velocity field (u, v) defined by $u = a \cos \phi \frac{d\lambda}{dt}$ and $v = a \frac{d\phi}{dt}$. Let f denote the Coriolis parameter, $2\Omega \sin \phi$, with Ω the angular velocity of the earth, a the radius of the earth, and g the gravitational constant. The SWEs on the sphere in flux form can then be formulated as

$$\frac{\partial H}{\partial t} + \nabla \cdot (H\underline{u}) = 0, \tag{2.1}$$

$$\frac{\partial Hu}{\partial t} + \nabla \cdot (Hu\,\underline{u}) = \left(f + \frac{u}{a} \tan \phi \right) Hv - \frac{gH}{a \cos \phi} \frac{\partial h}{\partial \lambda}, \tag{2.2}$$

$$\frac{\partial Hv}{\partial t} + \nabla \cdot (Hv\,\underline{u}) = -\left(f + \frac{u}{a} \tan \phi \right) Hu - \frac{gH}{a} \frac{\partial h}{\partial \phi}, \tag{2.3}$$

where the divergence operator is defined by

$$\nabla \cdot \underline{u} \equiv \frac{1}{a \cos \phi} \left[\frac{\partial u}{\partial \lambda} + \frac{\partial v \cos \phi}{\partial \phi} \right].$$

The right-hand sides in the momentum equations (2.2) and (2.3) represent, respectively, the Coriolis force, the hydrostatical pressure gradient force, and an additional term due to the relative motion in the rotating coordinate system in longitudinal and latitudinal direction, see [10].

2.2. The Shallow Water Equations in Stereographic Coordinates

The spherical formulation of the SWEs (2.1)–(2.3) has the disadvantage that it is singular at the poles. To circumvent this problem, the SWEs can be formulated in the stereographic coordinate system using a different stereographic projection on each hemisphere. Since these projections are only singular in opposite poles, no singularity problem arises. We note that the stereographic projection is conformal, so the general form of the equations is preserved.

The stereographic projection in terms of the latitude-longitude coordinates is defined by

$$x_{\text{st}} = a\,m \cos \phi \cos \lambda, \tag{2.4}$$

$$y_{\text{st}} = a\,m \cos \phi \sin \lambda, \tag{2.5}$$

where m is the map factor

$$m = \frac{2}{1 + \alpha \sin \phi}, \tag{2.6}$$

with α distinguishing between the northern ($\alpha = 1$) and the southern hemisphere projection ($\alpha = -1$). The poles are directly projected onto the origin of the stereographic planes. The northern hemisphere is projected from the south pole onto the northern stereographic plane, which is the plane locally tangent to the sphere at the north pole; see Fig. 1. Likewise, the southern hemisphere is projected from the north pole onto the southern stereographic plane, which is locally tangent to the sphere at the south pole. A description of the construction of the stereographic projection can be found in Appendix A of [11]. Note that the positive stereographic x_{st} axis for both the northern and the southern hemisphere corresponds with the intersection of the half-plane $S_{\lambda=0}$ and the corresponding stereographic plane. Likewise, the positive stereographic y_{st} axis corresponds, for both hemispheres, with the intersection of the half-plane $S_{\lambda=\pi/2}$ and the corresponding stereographic plane. Before we give the SWEs in the stereographic formulation, as found, for instance, in [2, 16, 26], we need to define the velocity field in the new stereographic coordinate system. Let $\underline{U} = (U, V)$ be the velocity field in stereographic coordinates with U the velocity in the x_{st} direction and V the
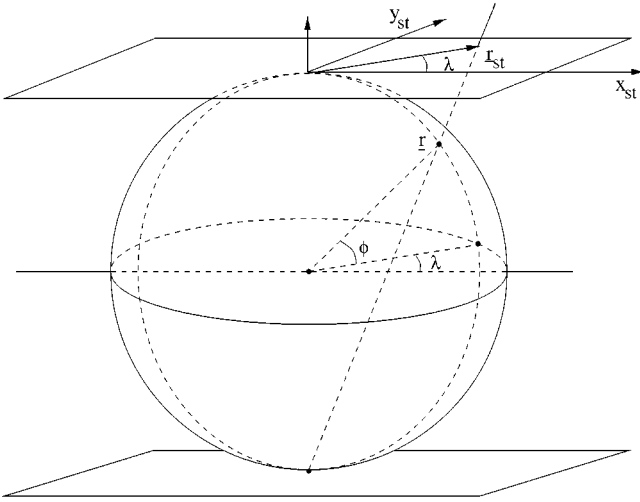
FIG. 1. The stereographic planes for the northern and southern hemisphere projections.

velocity in y_{st} direction. We have

$$\underline{U} = \begin{pmatrix} U \\ V \end{pmatrix} = \begin{pmatrix} m^{-1} \frac{dx_{st}}{dt} \\ m^{-1} \frac{dy_{st}}{dt} \end{pmatrix},$$

where $\frac{dx_{st}}{dt}$, $\frac{dy_{st}}{dt}$ are the usual total derivatives and $\frac{1}{m}$ is a scale factor with m as given in (2.6). When we now consider the momentum equations in the stereographic x_{st} and y_{st} directions, the stereographic formulation of the SWEs in flux form reads

$$\frac{\partial H}{\partial t} + \nabla \cdot (H\underline{U}) = 0, \tag{2.7}$$

$$\frac{\partial HU}{\partial t} + \nabla \cdot (HU\underline{U}) = \left[\alpha f - \frac{(x_{st}V - y_{st}U)}{2a^2} \right] HV - mgH \frac{\partial h}{\partial x_{st}}, \tag{2.8}$$

$$\frac{\partial HV}{\partial t} + \nabla \cdot (HV\underline{U}) = -\left[\alpha f - \frac{(x_{st}V - y_{st}U)}{2a^2} \right] HU - mgH \frac{\partial h}{\partial y_{st}}, \tag{2.9}$$

where the divergence operator is defined by

$$\nabla \cdot (A\underline{U}) \equiv m^2 \frac{\partial}{\partial x_{st}} \left(\frac{AU}{m} \right) + m^2 \frac{\partial}{\partial y_{st}} \left(\frac{AV}{m} \right). \tag{2.10}$$

This formulation is derived in Appendix B of [11].

To complete the discussion on the two different coordinate systems, we here give the relations between the stereographic and spherical velocity components,

$$U = -u \sin \lambda - \alpha v \cos \lambda, \tag{2.11}$$

$$V = u \cos \lambda - \alpha v \sin \lambda. \tag{2.12}$$

These relations, which of course are valid only outside the poles, are needed in Section 3.2.4.

3. SPATIAL DISCRETIZATION

In the past, several types of grids have been proposed to circumvent the problems related to solving the SWEs on a global lat–lon grid. Two examples are the composite cubic grid [17, 18] and the icosahedral grid [24]. The first yields a nonconformal mapping of the sphere onto a cube. The latter grid consists of triangles.

In this section we introduce another grid. Our motivation is to provide a grid on which calculations are simple and straightforward. Therefore we aim at a grid distribution which can be conformally mapped onto a rectangular computational domain without any singular points.

3.1. Using Stereographic Grids

Over the years several suggestions have been made to circumvent the singularity problem which arises at the poles when one tries to solve the SWEs in spherical coordinates. In 1956 Phillips [16] studied this problem. He suggested covering the sphere with three different coordinate systems. On part of the northern as well as on the southern hemisphere he used a stereographic coordinate system centered at the poles. In between those two regions he chose a mercator projection. His distribution of the coordinate systems is illustrated in Fig. 2a. To couple the different coordinate systems, Phillips had to interpolate from points in neighboring grids whenever a variable outside the current grid part was needed. In 1975 Stoker [22] showed that these interpolations could contribute to loss of mass.

In 1977 Starius [21] introduced the composite mesh method. Like Phillips, he used multiple coordinate systems, but he avoided interpolations within neighboring grids by letting the grids, corresponding with the different coordinate systems, overlap. To prosper from both methods, Browning *et al.* [2] combined the ideas of Starius and Phillips. They applied the composite mesh method to the SWEs by using two stereographic coordinate systems centered respectively at the north and south pole and extended beyond the equator.

Our approach is also based on the ideas of Phillips; that is, we use three different nonoverlapping coordinate systems, where stereographic coordinate systems are applied in the northern and southern polar areas. In the intermediate region, however, our choice of the


(a) (I) northern hemisphere stereographic projection
(II) mercator projection
(III) southern hemisphere stereographic projection

(b) (I) northern hemisphere stereographic projection
(II) spherical coordinate system
(III) southern hemisphere stereographic projection

FIG. 2. Distribution of the three different coordinate systems in Phillips' approach (a) and our approach (b).

coordinate system differs from Phillips'. Since spherical coordinates are natural and easily implemented in regions away from the poles, we prefer a spherical coordinate system in the intermediate region. Furthermore, lat–lon grids are still standard in meteorological applications. A further differentiation from the Phillips method concerns the coupling of the different coordinate systems. Although this subject is not addressed until Section 3.2, we state here that with our choice of a finite volume method we are able to avoid the interpolation problems found by Phillips. Our distribution of the coordinate systems is shown in Fig. 2b.

In this paragraph we discuss the exact distribution of the three different coordinate systems across the sphere. As mentioned before, we prefer to use a lat–lon grid in a region away from the poles. We define this region as $R_{II} = \{(\lambda, \phi, a): \lambda \in [0, 2\pi), \phi \in [-\bar{\phi}, \bar{\phi}]$ with $\bar{\phi} < \frac{\pi}{2}\}$. From an illustrative point of view we assume that our lat–lon grid has a uniform distribution. Note that more advanced grid distributions are possible. In Section 4, for instance, we apply a reduced lat–lon grid. To find a suitable grid distribution in the stereographic regions, we project the uniform lat–lon grid of region R_{II} onto the stereographic planes, as illustrated for one hemisphere in Fig. 3. Note that meridians and parallels correspond with respectively dashed and solid lines. In the middle of the resulting projection we place a square with bottom left-hand corner $(x_{st}, y_{st}) = (-x_r, -x_r)$ and top right-hand corner $(x_{st}, y_{st}) = (x_r, x_r)$, $x_r > 0$. The corresponding regions on the sphere are denoted by region I (northern hemisphere) and III (southern hemisphere). To secure a proper fit between the grids on regions I, III, and R_{II}, we extend the projected meridians until they intersect with the squares. The resulting cells between these regions are added to region R_{II} giving the region II shown in Fig. 2b. The solid lines in Fig. 4 correspond with the cell edges. We then demand that N_λ defined as $N_\lambda = \frac{1}{\Delta\lambda}$ is a multiple of eight. Under this condition the intersection points have mirror images on the opposite edge. After these points are connected, a nonuniform rectangular grid distribution on the square results; see Fig. 4a. The total grid distribution over the sphere is now fully known; see Fig. 4b. Finally, we remark that x_r, N_λ and $\bar{\phi}$ are still free parameters. Exact values are given for each test case. These values affect, for instance, the CFL number, the meshwidth
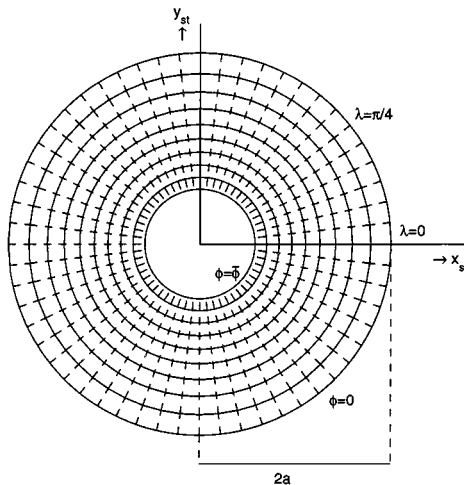
FIG. 3. Northern hemisphere projection from the south pole of a uniform lat–lon grid. Dashed lines correspond with meridians (λ constant). Solid lines correspond with parallels (ϕ constant).
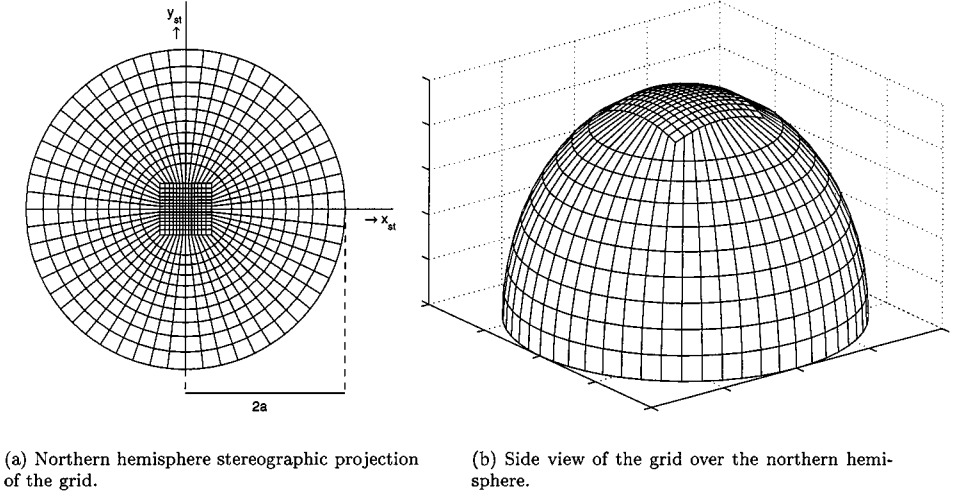
(a) Northern hemisphere stereographic projection of the grid.

(b) Side view of the grid over the northern hemisphere.

FIG. 4. Different views of the grid distribution over the northern hemisphere.

factors, and the accuracy. For visualization purposes we used $N_\lambda = 56$, $x_r = 0.32279\, a$, and $\bar{\phi} = 57.8°$.

3.2. The Semi-Discrete System in General Terms

Without the Coriolis and additional forces, the SWEs closely resemble the Euler equations, which can be found in, for instance, gas dynamic applications. For the full set of primitive equations this resemblance is even more explicit. Much theory concerning the space discretization of the Euler equations has already been developed; see, for instance, [9]. In our approximation method we gratefully adopt existing ideas from this theory. In this section we will describe the semi-discrete system for the SWEs (2.1)–(2.3) and (2.7)–(2.9) with special attention to the coupling between the spherical and stereographic grids.

3.2.1. Main Outline of the Finite Volume Method

We begin this section with a main outline of our method. To guarantee conservation of mass and momentum in our semi-discrete system or, in other words, to respect the underlying physical conservation laws, we use the finite volume method, which is standard practice for the Euler equations. We focus on the stereographic region I. Similar results can be derived for the spherical region II and for region III. Calculations are done in the computational domain, which results after projection of regions I, II, and III on the regions associated with the corresponding coordinate systems. In the computational domains regular, (non-)uniform rectangular grids occur.

Let $\Omega_{i,j}$ be a grid cell with boundary $\delta\Omega_{i,j}$. We denote its four neighbors by $\Omega_{i\pm1,j}$ and $\Omega_{i,j\pm1}$. The boundary between two neighboring cells, for instance, between $\Omega_{i+1,j}$ and $\Omega_{i,j}$, is denoted by $\delta\Omega_{i+1/2,j}$. $\underline{n}_{i+1/2,j} = (n_{x_{st}}, n_{y_{st}})$ is the outwardly directed unit normal along this boundary. $\Delta x_{i,j}$ and $\Delta y_{i,j}$ are respectively the lengths of $\delta\Omega_{i,j\pm1/2}$ and $\delta\Omega_{i\pm1/2,j}$; see Fig. 5. We associate with each grid cell its cell center $\underline{x}_{st_{i,j}} = (x_{st_{i,j}}, y_{st_{i,j}})$ with state variable $\underline{q}_{i,j} = (H_{i,j}, H_{i,j}U_{i,j}, H_{i,j}V_{i,j})$ and we assume that the state variable is constant over each
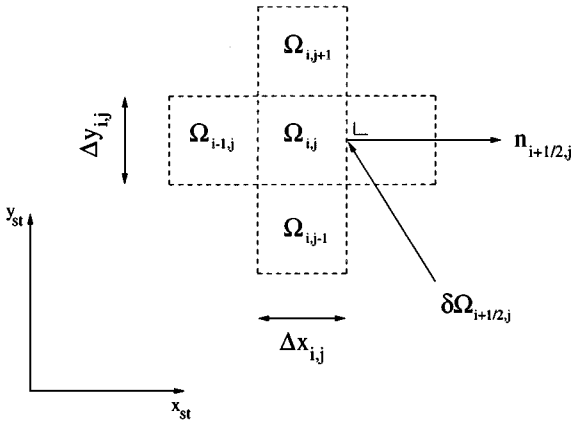
FIG. 5. The grid cell $\Omega_{i,j}$ in the stereographic coordinate system.

cell. The finite volume method now gives

$$\frac{\partial \underline{q}_{i,j}}{\partial t} + \frac{m_{i,j}^2}{\Delta x_{i,j} \Delta y_{i,j}} \oint_{\delta\Omega_{i,j}} \frac{1}{m}\underline{F}n_{x_{\mathrm{st}}} + \frac{1}{m}\underline{G}n_{y_{\mathrm{st}}}\, dS = -\left(\underline{f}_{x_{\mathrm{st}}}(\underline{q}_{i,j}, \underline{x_{\mathrm{st}}}_{i,j}) + \underline{f}_{y_{\mathrm{st}}}(\underline{q}_{i,j}, \underline{x_{\mathrm{st}}}_{i,j})\right),$$

$$(3.1)$$

where $\underline{F}$ and $\underline{G}$ are the fluxes in stereographic x_{st} and y_{st} direction,

$$\underline{F}(\underline{q}) = \left(HU, HU^2 + \frac{1}{2}gH^2, HUV\right)^T,$$

$$\underline{G}(\underline{q}) = \left(HV, HUV, HV^2 + \frac{1}{2}gH^2\right)^T,$$

and

$$\underline{f}_{x_{\mathrm{st}}}(\underline{q}, \underline{x_{\mathrm{st}}}) = \left(0, -\left[\alpha f - \frac{(x_{\mathrm{st}}V - y_{\mathrm{st}}U)}{2a^2}\right]HV + mgH\frac{\partial h_s}{\partial x_{\mathrm{st}}} + \frac{1}{4a^2}gH^2 x_{\mathrm{st}}, 0\right)^T,$$

$$\underline{f}_{y_{\mathrm{st}}}(\underline{q}, \underline{x_{\mathrm{st}}}) = \left(0, 0, \left[\alpha f - \frac{(x_{\mathrm{st}}V - y_{\mathrm{st}}U)}{2a^2}\right]HU + mgH\frac{\partial h_s}{\partial y_{\mathrm{st}}} + \frac{1}{4a^2}gH^2 y_{\mathrm{st}}\right)^T.$$

To respect the characteristic directions associated with the hyperbolic character of our equations, we apply an upwind scheme to discretize the integral in (3.1). Within the group of finite volume upwind methods we distinguish two different categories, concerning flux vector splitting (FVS) and flux difference splitting (FDS) methods. For a detailed description of both methods we refer to [9]. Methods from the first category do not suffice as discretization schemes when applied to the SWEs. The condition that the Jacobian of the flux vector $\underline{F}$ with respect to $\underline{q}$ is homogeneous of degree 1 (see [9]) is not fulfilled. We apply Osher's approximate Riemann solver [14, 15], which makes an excellent choice from the group of FDS methods. Osher's scheme is robust and second-order accurate, when combined with the right state interpolation [23]. Furthermore, from a future perspective, it has a logical extension to more realistic primitive equations and a consistent boundary treatment.

The last argument made us decide in favor of Osher's approximate Riemann solver before Roe's, which is often used in gas dynamics applications.

The semi-discrete system reads

$$
\begin{aligned}
\frac{\partial \underline{q}_{i,j}}{\partial t} &+ \frac{m_{i,j}^2}{\Delta x_{i,j} \Delta y_{i,j}} \left[T^{-1}(0) \underline{F}_{(O)} \left(T(0) \underline{q}_{i+\frac{1}{2},j}^{\mathrm{L}}, T(0) \underline{q}_{i+\frac{1}{2},j}^{\mathrm{R}} \right) \frac{\Delta y_{i,j}}{m_{i+\frac{1}{2},j}} \right. \\
&+ T^{-1}\left(\frac{\pi}{2}\right) \underline{F}_{(O)} \left(T\left(\frac{\pi}{2}\right) \underline{q}_{i,j+\frac{1}{2}}^{\mathrm{L}}, T\left(\frac{\pi}{2}\right) \underline{q}_{i,j+\frac{1}{2}}^{\mathrm{R}} \right) \frac{\Delta x_{i,j}}{m_{i,j+\frac{1}{2}}} \\
&+ T^{-1}(\pi) \underline{F}_{(O)} \left(T(\pi) \underline{q}_{i-\frac{1}{2},j}^{\mathrm{L}}, T(\pi) \underline{q}_{i-\frac{1}{2},j}^{\mathrm{R}} \right) \frac{\Delta y_{i,j}}{m_{i-\frac{1}{2},j}} \\
&+ \left. T^{-1}\left(\frac{3\pi}{2}\right) \underline{F}_{(O)} \left(T\left(\frac{3\pi}{2}\right) \underline{q}_{i,j-\frac{1}{2}}^{\mathrm{L}}, T\left(\frac{3\pi}{2}\right) \underline{q}_{i,j-\frac{1}{2}}^{\mathrm{R}} \right) \frac{\Delta x_{i,j}}{m_{i,j-\frac{1}{2}}} \right] \\
&= -\left(\underline{f}_{x_{\mathrm{st}}} \left(\underline{q}_{i,j}, \underline{x}_{\mathrm{st}\,i,j} \right) + \underline{f}_{y_{\mathrm{st}}} \left(\underline{q}_{i,j}, \underline{x}_{\mathrm{st}\,i,j} \right) \right),
\end{aligned}
\tag{3.2}
$$

where $T(\theta)$ is a rotation matrix defined by

$$
T(\theta) = \begin{pmatrix} 1 & 0 & 0 \\ 0 & \cos\theta & \sin\theta \\ 0 & -\sin\theta & \cos\theta \end{pmatrix}
\tag{3.3}
$$

and $\underline{F}_{(O)}$ is the Osher flux given as

$$
\underline{F}_{(O)}(\underline{q}^{\mathrm{L}}, \underline{q}^{\mathrm{R}}) = \frac{1}{2} (\underline{F}(\underline{q}^{\mathrm{L}}) + \underline{F}(\underline{q}^{\mathrm{R}})) - \frac{1}{2} \int_{\underline{q}^{\mathrm{L}}}^{\underline{q}^{\mathrm{R}}} |A(\underline{q})| \, d\underline{q}.
\tag{3.4}
$$

A is here defined as the Jacobian of the fluxvector $\underline{F}$ with respect to $\underline{q}$, $A = \partial \underline{F}/\partial \underline{q}$. The absolute value of this Jacobian is defined by

$$
|A(\underline{q})| = P(\underline{q}) |\Lambda| P^{-1}(\underline{q}),
$$

where P and Λ result from diagonalizing the Jacobian matrix as $A = P\Lambda P^{-1}$. Note that the Osher fluxes in (3.2) describe local fluxes; i.e., they point in the direction of the outwardly directed unit normal on the corresponding boundary. The Osher flux (3.4) approximates the local flux across a boundary $\delta\Omega$, which results when at the left and the right of this boundary the constant states $\underline{q}^{\mathrm{L}}$ and $\underline{q}^{\mathrm{R}}$ are found.

So far, we have not mentioned the evaluation of the constant states. It is through these evaluations that we are able to properly couple the different grids. Furthermore, the state evaluations determine the accuracy of our scheme. On a uniform grid, second-order accuracy can be proven [19]. We attend to this topic in the next section. It remains to say that the Osher scheme is special for its choice of the integration path in its flux (3.4). Using the Osher flux boils down to a maximum of five flux evaluations, $\underline{F}(\underline{q})$, per cell boundary. In the case of the most common atmospheric flow patterns, i.e., flows where we have $|u| \leq \sqrt{gH}$, we find that the Osher flux requires only one flux evaluation per cell boundary, when we use the P-variant Osher path suggested by Hemker and Spekreijse [8]. Details of the construction of the integration path and the Osher flux can be found in Appendix C of [11].

3.2.2. *Determination of the Constant States*

In this section we define the constant states. We still focus on the stereographic region zooming in on the state evaluation in the x_{st} direction. The states in the y_{st} direction are defined in a similar way. We apply 1D state interpolation; i.e., the state $q^L_{i+\frac{1}{2},j}$ only depends on the states of neighboring cells in the x_{st} direction. For the remaining part of this section, we suppress the index j in our notation. To define the constant states, we use the $(\kappa = 1/3)$ scheme [23]. On a uniform grid it reads

$$
\begin{aligned}
\underline{q}^L_{i+\frac{1}{2}} &= \underline{q}_i + \frac{(1-\kappa)}{4}(\underline{q}_i - \underline{q}_{i-1}) + \frac{(1+\kappa)}{4}(\underline{q}_{i+1} - \underline{q}_i), \\
\underline{q}^R_{i+\frac{1}{2}} &= \underline{q}_{i+1} + \frac{(1-\kappa)}{4}(\underline{q}_{i+1} - \underline{q}_{i+2}) + \frac{(1+\kappa)}{4}(\underline{q}_i - \underline{q}_{i+1}).
\end{aligned}
\tag{3.5}
$$

Unfortunately, our grid in the projected stereographic region is nonuniform. When the grid is sufficiently smooth, this discrepancy is often circumvented by simply applying the existing κ scheme (3.5). Although this condition holds for our grid, we do not adopt this approach. We wish to avoid any additional errors which might prevent us from properly identifying the influence of the coupling between the different grids. Therefore, we have applied a modification of the κ scheme (3.5) for nonuniform grids. The general form of this modified κ scheme can be found in Appendix D of [11] for different values of κ. The general form is defined as a function, I_κ, with the states and cell widths of neighboring grid cells in the interpolation direction as arguments. The standard nonuniform state interpolation is represented in Table I.

Near the grid interface between the stereographic and the spherical region (see Fig. 4a), the stencil of the nonuniform $(\kappa = 1/3)$ scheme is too large, demanding state variables from outside the stereographic region. To avoid transformations and difficulties associated with the kink in the grid cells, we regard the grid interface as a real boundary. This means that locally we have to reduce the size of our stencil. To that end we have also formulated the nonuniform equivalents of the 2-point central $(\kappa = 1)$ scheme, the 2-point upwind $(\kappa = -1)$ scheme, and the 3-point upwind $(\kappa = 1/2)$ scheme. Figure 6 shows which interpolation scheme is applied on each cell boundary. The associated state interpolations are given in

TABLE I
The Different State Interpolation Methods Used Near the Grid Boundary

	Left	Right
A	$\underline{q}^L_{\frac{1}{2}} = $ Transformation	$\underline{q}^L_{N+\frac{1}{2}} = I_{-1}(\underline{q}_{N-1}, \underline{q}_N, \ell_{N-1}, \ell_N)$
	$\underline{q}^R_{\frac{1}{2}} = I_{-1}(\underline{q}_2, \underline{q}_1, \ell_2, \ell_1)$	$\underline{q}^R_{N+\frac{1}{2}} = $ Transformation
B	$\underline{q}^L_{\frac{3}{2}} = I_1(\underline{q}_1, \underline{q}_2, \ell_1, \ell_2)$	$\underline{q}^L_{N-\frac{1}{2}} = I_{\frac{1}{2}}(\underline{q}_{N-2}, \underline{q}_{N-1}, \underline{q}_N, \ell_{N-2}, \ell_{N-1}, \ell_N)$
	$\underline{q}^R_{\frac{3}{2}} = I_{\frac{1}{2}}(\underline{q}_3, \underline{q}_2, \underline{q}_1, \ell_3, \ell_2, \ell_1)$	$\underline{q}^R_{N-\frac{1}{2}} = I_1(\underline{q}_N, \underline{q}_{N-1}, \ell_N, \ell_{N-1})$
C	$\underline{q}^L_{\frac{5}{2}} = I_{\frac{1}{2}}(\underline{q}_1, \underline{q}_2, \underline{q}_3, \ell_1, \ell_2, \ell_3)$	$\underline{q}^R_{N-\frac{3}{2}} = I_{\frac{1}{2}}(\underline{q}_N, \underline{q}_{N-1}, \underline{q}_{N-2}, \ell_N, \ell_{N-1}, \ell_{N-2})$
D	$\underline{q}^L_{i+\frac{1}{2}} = I_{\frac{1}{3}}(\underline{q}_{i-1}, \underline{q}_i, \underline{q}_{i+1}, \ell_{i-2}, \ell_{i-1}, \ell_i, \ell_{i+1}, \ell_{i+2})$,	
	$\underline{q}^R_{i+\frac{1}{2}} = I_{\frac{1}{3}}(\underline{q}_{i+2}, \underline{q}_{i+1}, \underline{q}_i, \ell_{i+3}, \ell_{i+2}, \ell_{i+1}, \ell_i, \ell_{i-1})$	

Note. The indices A, B, C, and D here correspond with the different cell boundary situations illustrated in Fig. 6.
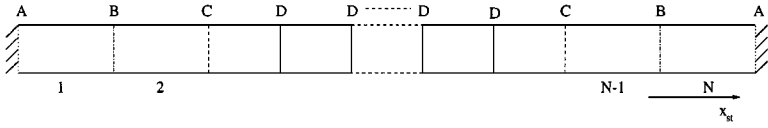
FIG. 6. Illustration of the cell boundaries, where interpolation scheme other than standard is needed.

Table I. Note that although it is a 3-point interpolation scheme, the ($\kappa = 1/3$) scheme, as opposed to the ($\kappa = 1/2$) scheme, cannot be applied at the cell boundaries $\delta\Omega_{5/2}$ and $\delta\Omega_{N-3/2}$, because in these cases a cell width from outside the stereographic region is needed. In the next section, we will discuss the transformation entry in Table I.

3.2.3. *The Finite Volume Method and the Constant States on the Spherical Computational Domain*

The same line of semi-discretization as described in Section 3.2.1 is applied to derive the semi-discrete system for region II; see Fig. 2b. Note that for this region calculations are done on the (λ, ϕ) plane. The semi-discrete system easily follows through Eqs. (3.2)–(3.4) when we replace $m_{i,j}$, $\Delta x_{i,j}$, $\Delta y_{i,j}$, $\underline{f}_{x_{st}}$, $\underline{f}_{y_{st}}$, and $\underline{q}$ successively by $1/(a \cos \phi_{i,j})$, $\Delta \lambda_{i,j}$, $\Delta \phi_{i,j}$, $\underline{f}_{\lambda}$, $\underline{f}_{\phi}$, and $\underline{q} = (H, \ Hu, \ Hv)$, where

$$\underline{f}_{\lambda}(\underline{q}, \underline{r}) = \left(0, -\left(f + \frac{u}{a} \tan \phi\right) Hv + \frac{gH}{a \cos \phi}\frac{\partial h_s}{\partial \lambda}, 0\right)^T,$$

$$\underline{f}_{\phi}(\underline{q}, \underline{r}) = \left(0, 0, \left(f + \frac{u}{a} \tan \phi\right) Hu + \frac{gH^2 \sin \phi}{2a \cos \phi} + \frac{gH}{a}\frac{\partial h_s}{\partial \phi}\right)^T.$$

Note that the form of the flux vectors $\underline{F}$ and $\underline{G}$ remains the same, since both coordinate systems are conformal.

To evaluate the constant states on region II we again use 1D state interpolation. This time it concerns interpolation in the λ or ϕ direction depending on the cell boundary under consideration. As standard interpolation scheme the ($\kappa = 1/3$) scheme is applied. In the λ direction this scheme can be applied everywhere, because, in that direction, our grid is uniform and has no grid boundaries. In the ϕ direction we have to account for the grid interface between the spherical and the stereographic grids. We treat this interface as if it concerns a piecewise constant real boundary approximating the cell boundaries by the lines $\phi = \phi_{i,N_\phi+1/2}$; see Fig. 7. The resulting, partially nonuniform grid distribution resembles the one in the stereographic direction. Therefore, the associated state interpolations easily follow by applying Table I in the ϕ direction.

3.2.4. *Interaction between the Different Computational Domains*

It remains to discuss the transformation entry in Table I. We again turn to the stereographic computational domain associated with region I and focus on the x_{st} direction; see Fig. 6. At the grid interface between region I and II the computational domains of these regions interact. To find the states $\underline{q}^L_{1/2}$ and $\underline{q}^R_{N+1/2}$ in stereographic variables, we transform the states in spherical variables found at the same cell interface boundary in the computational domain associated with region II. The word "transformation" here indicates that we must convert
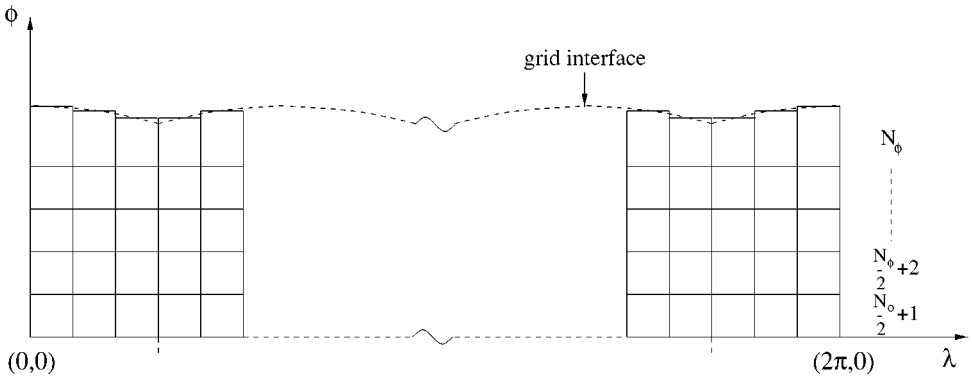
FIG. 7. Projection of the northern hemisphere part of region II on the (λ, ϕ) plane in combination with the approximated cell distribution at the grid boundary.

the velocity field $\underline{u} = (u, v)$ into its stereographic representation. Note that the constant states in spherical variables are calculated by one-sided ($\kappa = -1$)-state interpolation in the ϕ direction. This way of state evaluation yields that at every cell interface boundary, the 1D state interpolation to obtain $q^L_{1/2}$ and $q^R_{N+1/2}$ is performed in a different direction, i.e., in the direction of the projected meridians $\lambda_{1/2}$ and $\lambda_{N+1/2}$. In the case of interpolations in the ϕ direction, the transformation entries, i.e., $\underline{q}^L_{1/2}$ and $\underline{q}^R_{N_\phi+1/2}$ in spherical variables, follow after transformatoin of the corresponding constant states in stereographic variables found at the same cell boundaries in the computational domain of region I. Here the word "transformation" means that we must convert the velocity field $\underline{U} = (U, V)$ into its spherical equivalent. Note that, depending on the cell's position, the constant state in stereographic variables concerns a constant state calculated by one-sided ($\kappa = -1$)-state interpolation in x_{st} or y_{st} direction.

We conclude this section with some remarks on accuracy. In more dimensional problems a finite volume method is at most second-order accurate. To provide an order estimate we cite Spekreijse [19]. For a uniform grid, he proved, that a scheme like (3.2) is second-order accurate for interpolations based on the κ scheme. On a large part of our domain, i.e., almost everywhere on the spherical region (see Section 3.2.3), his estimate is valid, because our grid is uniform. However, since we combine different grids, it is difficult to give the exact order of our scheme across the whole sphere. It is obvious that we endure some accuracy loss around the interface, which will be referred to as the connection problem. To be conclusive about its severity, we will give a numerical order estimate in Section 4.

4. NUMERICAL TESTS

In this section we focus on two main objectives. First, we wish to establish to what extent the introduction of the stereographic grid resolves the problems related to the use of a global spherical coordinate system. Second, we wish to validate our spatial discretization scheme or, in other words, how Osher's scheme behaves, when applied to the SWEs on the sphere, and how accurate its results are.

To meet the necessity of a good benchmark to test new numerical methods for solving the SWEs in spherical geometry, Williamson *et al.* [27] developed a test set, containing seven different test cases of increasing complexity. We concentrate on test case 2 of this test

set, i.e., on the global steady state nonlinear zonal geostrophic flow. Test case 2 provides us with a good test to examine the scheme's ability to handle the poles. Furthermore, it serves as a test for our Osher scheme, since it includes nonlinear aspects of the SWEs. As holds for the whole test set, test case 2 is not entirely appropriate to demonstrate all favorable features of our scheme, i.e., its behavior around strong gradients. The problems in the test set have solutions with rather smooth flow patterns. Hence it is suitable for a first assessment of accuracy behavior. Besides test case 2, we successfully solved test cases 1 and 6, i.e., advection of a cosine bell over the pole and the Rossby–Haurwitz wave. To save space we present results only for test case 2. In future work we will attend to the other cases.

4.1. Test Case 2: Global Steady State Nonlinear Zonal Geostrophic Flow

Test case 2 concerns a steady-state analytic solution to the non-linear SWEs. It consists of a solid body rotation with the corresponding geostrophic height field H. A parameter α is used to specify the angle between the axis of the solid body rotation and the polar axis of the spherical coordinate system: $\alpha = 0$ indicates equatorial flow and $\alpha = \pi/2$ yields flow across the pole. The analytic solution of test case 2 reads

$$H = h_0 - \left(\frac{a\Omega u_0}{g} + \frac{u_0^2}{2g} \right)(-\cos\lambda\cos\phi\sin\alpha + \sin\phi\cos\alpha)^2, \tag{4.1}$$

$$u = u_0(\cos\phi\cos\alpha + \sin\phi\cos\lambda\sin\alpha), \tag{4.2}$$

$$v = -u_0\sin\lambda\sin\alpha, \tag{4.3}$$

where the Coriolis parameter $f = 2\Omega\,(-\cos\lambda\cos\phi\sin\alpha + \sin\phi\cos\alpha)$ and $u_0 = 38.61$ m/s, $h_0 = 3.00 \times 10^3$ m. To be consistent with the article of Williamson *et al.* [27], we tested our code for $\alpha = 0, 0.05, \pi/2 - 0.05$, and $\pi/2$, where the second and third parameter values were added to avoid symmetries. In this article we will not present all the results, as our code produced good results for either value. We will concentrate on tests with parameter value $\alpha = \pi/2$, since for these tests the corresponding velocity components initiate the strongest flow across the poles. We remark that these kind of flows can indeed be encountered in practical situations.

In addition to the fact that we encounter a singularity problem when we apply the spherical formulation of the SWEs in the poles, we have to deal with some problems when approaching the poles. Figure 8 clearly illustrates the demand for additional caution near the poles. This figure represents the analytic longitudinal and latitudinal velocity components, u and v, found in the cell centers of an underlying uniform lat–lon grid in case of flow across the poles ($\alpha = \pi/2$). To emphasize our point we give the velocity components u and v, which follow from (4.1)–(4.3),

$$u = u_0\sin\phi\cos\lambda, \tag{4.4}$$

$$v = -u_0\sin\lambda. \tag{4.5}$$

The figure shows that the spherical velocity components strongly vary in the polar area, bringing about difficulties in numerical approximation methods. To properly represent these velocity components, a fine grid resolution, especially in the longitudinal direction, is necessary. However, too many grid cells can lead to problems for integration methods related to stability.
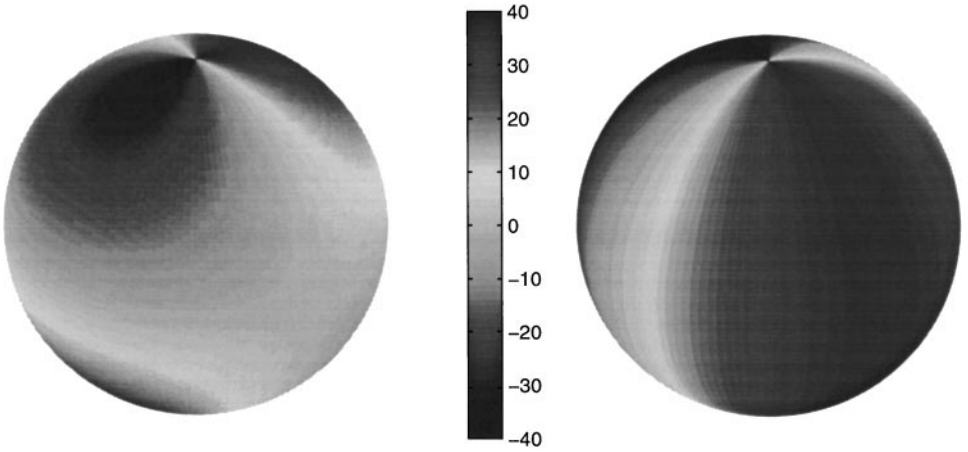
FIG. 8. Representation of the analytic longitudinal velocity component u (left) and latitudinal velocity component v (right) on a global uniform lat–lon grid in case of global steady-state nonlinear zonal geostrophic flow across the pole ($\alpha = \pi/2$).

We discuss two remedies to these approximation and stability problems. First, we can decide to solve the SWEs on a stereographic grid. On a stereographic grid no severe resolution problems arise, as the velocity components U and V vary much less than the spherical ones; see Fig. 9. Second, we can consider the reduced grid approach. In that case, the lat–lon grid is coarsened in the longitudinal direction at given latitudes (for details, see [1, 25]). Both remedies suffer some problems though. On a stereographic grid, we are confronted with a connection problem at the equator when we try to combine the stereographic grids on the northern and southern hemispheres (see Fig. 9). On a (nearly) global lat–lon grid, we are not allowed to apply the reduced grid approach to its fullest extent. Repeated reductions to arrive, for instance, at four remaining grid cells next to the poles are inadmissible, since in that case the grid near the poles is too coarse to represent the strongly varying velocity components. With a combination of both remedies, i.e., a combined grid with a reduced
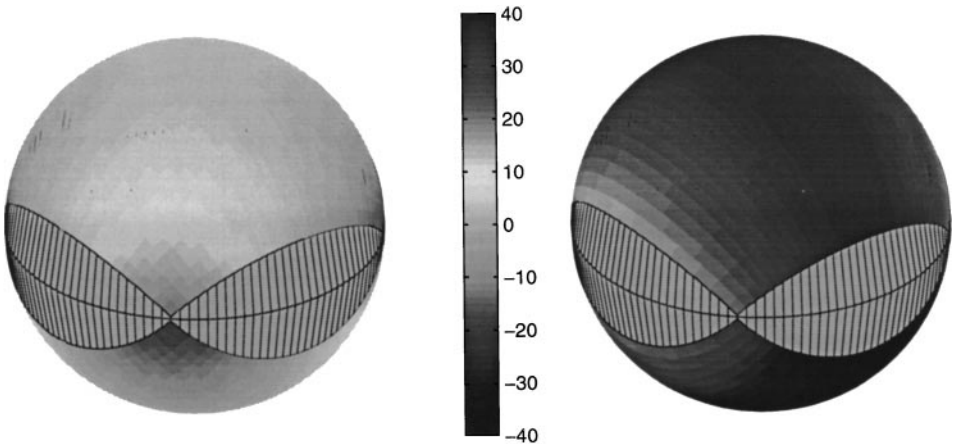
FIG. 9. Representation of the analytic stereographic velocity components U (left) and V (right) on a "global" uniform stereographic grid in case of global steady state nonlinear zonal geostrophic flow across the pole.
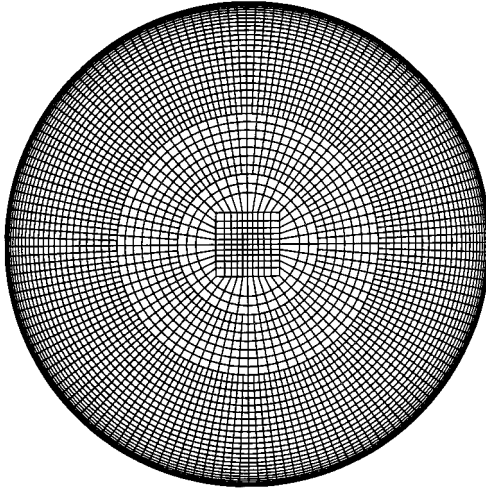
FIG. 10. Projection of a combined grid consisting of a reduced lat–lon grid away from the poles and a stereographic grid at the two polar caps onto the cartesian (x, y) plane $(z = 0)$. Two reductions were applied.

lat–lon grid away from the poles and a stereographic grid at the two polar caps, we can avoid these problems and benefit from either advantage (see Fig. 10).

In the remaining part of this section we will address the following questions concerning our grid. Do the numerical results confirm the problems suggested when calculating on a global reduced lat–lon grid? Which factors determine the actual form of a combined grid, or in other words, how large should the stereocap be and how many reductions are allowed? And, how accurate are the results when calculated on a combined grid with realistic refinement?

4.1.1. *Experiments on Global Lat–Lon Grids*

The pole singularity.   For tests on a global lat–lon grid to make sense, we must account for the nonexistence of the spherical fluxes $\underline{F}$ and $\underline{G}$ in the poles. In practice, this problem is overcome by assuming a total zero flux across the boundaries corresponding to the poles. The question is whether the results significantly suffer from this assumption, both near and away from the poles. In fact, when the results do suffer from this assumption, we should reconsider investigating the global reduced lat–lon grid, since the results would be inadequate without an accurate resolution of the singularity problem in the pole.

We first ran a set of tests on a rectangular global lat–lon grid, where we varied the amount of gridpoints in the ϕ direction, thus moving the neighboring cell centers closer to the pole with each test. Let nP define the amount of gridpoints in the ϕ direction and let $\Delta\phi = 180°/\text{nP}$. In comparison with other tests, our grid distribution in the λ direction is rather coarse (nL $= 72$). We must only make sure that the solution can be properly represented in that direction. In this way we are able to reduce computing time and avoid problems related to stability. The error measures on H are shown in Table II. For time stepping we used the fourth-order Runge–Kutta method with small steps, such that the error $E_r(H)$ represents the spatial discretization error. $E_r(H)$ is defined as a maximum relative error,

$$E_r(H) = \max_{(i,j)} \left| \frac{H_{i,j} - H(\lambda_i, \phi_j)}{H(\lambda_i, \phi_j)} \right|,$$

TABLE II
Error Measures on H for Different Values of nP Taken over the Volumes Located Next to the Poles and over the Whole Domain on a Rectangular Lat–Lon Grid (nL = 72)

	$E_r(H)_{\text{pole band}}$	$E_r(H)_{\text{whole}}$
nP = 36	$2.1 \cdot 10^{-3}$	$9.8 \cdot 10^{-3}$
nP = 72	$1.1 \cdot 10^{-3}$	$5.7 \cdot 10^{-3}$
nP = 180	$8.7 \cdot 10^{-4}$	$5.3 \cdot 10^{-3}$

where $H(\lambda_i, \phi_j)$ gives the analytic solution of H in cell center (i, j). The max-norm is taken over a specified region. Note that since $H \gg 1$, the relative error provides a good indication of the accuracy of our results.

Table II clearly shows that in the band next to the poles the zero flux assumption does not lead to an error increase when approaching the poles. We even observe a minor decrease and the (relative) error certainly is sufficiently small for practical purposes. Moreover, the error in the pole band is smaller than the error over the whole domain. Note that since nL is fixed, convergence of the Osher scheme is not examined in these tests.

Pole resolution problem. As mentioned before and as discussed by Williamson and Browning in [26], we encounter representation problems when we try to approximate the spherical velocity components on a too coarse grid around the poles. The following tests have been chosen to show the severity of this problem. We tested four different reduced rectangular lat–lon grids, all having nL(0) = 64 grid cells in the longitudinal direction and nP = 192 cells in latitudinal direction. nL(0) is here defined as the amount of grid cells in the longitudinal direction on the unreduced grid part. When approaching the poles, we halve the amount of grid cells in the longitudinal direction, whenever the cell width in that direction projected onto the sphere, i.e., $a \cos \phi \Delta \lambda$, is reduced with a factor two following the last reduction. The specific values for nL(0) = 64 and nP = 192 are chosen so that we can arrive on a coarse grid within a few reductions and for each grid part, containing the same amount of grid cells in longitudinal direction, enough grid cells in latitudinal direction are guaranteed. Successively, we apply one, two, three, or four reductions at the latitudes $\phi = 60°, 75.9375°, 82.5°$, and $86.25°$. The errors are displayed in Table III. This time we concentrate on the absolute error, $E_a(u)$, found for the velocity component u instead of for H, since this component suffers the most from the inadequacy to represent the flux

TABLE III
Error Measures on u Taken over the Whole Domain on a Global Reduced Lat–Lon Grid with Different Levels of Reduction (nL(0) = 64, nP = 192)

	$E_a(u)$	Grid part m
0 reductions,	0.32	0
1 reduction at $\phi = 60°$	1.03	$-1/1$
2 reductions resp. at $\phi = 60°, 75.9375°$	3.67	$-2/2$
3 reductions resp. at $\phi = 60°, 75.9375°, 82.5°$	15.18	$-3/3$
4 reductions resp. at $\phi = 60°, 75.9375°, 82.5°, 86.25°$	23.99	$-4/4$

Note. The second column displays on which grid part m the maximum error is located.

on a coarse lat–lon grid. Furthermore, the absolute error is shown, because the velocity component may vanish in certain points of the globe; see; (4.4) and (4.5). $E_a(u)$ is defined as the maximum absolute error

$$E_a(u) = \max_{i,j} |u_{i,j} - u(\lambda_i, \phi_j)|,$$

where $u(\lambda_i, \phi_j)$ represents the analytic velocity component u in cell center (λ_i, ϕ_j). The maximum is taken over the whole grid, where the second column entry indicates on which grid part m the maximum error is found. The index m denotes the grid part found between the $|m|$th and $(|m| + 1)$th reduction. We indicate the different grid parts at the northern hemisphere with positive values of m and at the southern hemisphere with negative values of m.

Given that the analytic longitudinal velocity component u has a maximum of 38.61 m/s, the results speak for themselves. It is obvious that a significant number of cells next to the poles are needed to properly represent the velocity components. For example, in this case and starting from nL(0) = 64, two reductions giving 16 cells next to the poles already result in a maximum relative error in the longitudinal velocity component u of about 10%. Note that the maximum errors are found in the grid part closest to the pole.

Order tests.   In this part we provide a numerical order estimate for our spatial discretization scheme. As described in Section 3.2.4, we expect to find second-order accuracy on a uniform grid. To verify this, we ran some tests on a global uniform lat–lon grid. We only performed calculations on a band between latitudes $\phi = -60°$ and $\phi = 60°$ to avoid small steps related to stability. On the other areas of the sphere we prescribed the analytic solution. Note that in this way accuracy losses due to the zero flux assumption across the poles are circumvented. Successively, we applied a uniform lat–lon grid with nL = 72, 144, 288 and 576. Table IV shows the relative error measures on H. We consider the max-norm over the band.

The order factor between two successive grids is given in the third column of Table IV. In the case of second-order accuracy this factor should be 4. For the higher orders observed, we have two possible explanations. First, the theoretical order estimate holds in the asymptotic case, i.e., when nL approaches infinity. The order factor between the grids with nL = 576 and nL = 288 already approaches 4. Second, on the band between the latitudes $\phi = -60°$ and $\phi = 60°$, the flow has a strongly one-dimensional character which coincides with the meridians. For a uniform grid Spekreijse [19] proved that a scheme like (3.2) is third-order accurate for interpolations based on the ($\kappa = 1/3$) scheme in the 1D case. This might explain why on the coarser grids our order factors are close to 8. Note that the value 5.1 can

TABLE IV
Error Measures on H for Different Values of nL Taken over a Band between the Latitudes $\phi = -60°$ and $\phi = 60°$ on a Global Uniform Lat–Lon Grid[a]

	$E_r(H)_{band}$	$\dfrac{E_r(H)_{band_{nL/2}}}{E_r(H)_{band_{nL}}}$
nL = 72	$2.05 \cdot 10^{-3}$	
nL = 144	$2.69 \cdot 10^{-4}$	7.6
nL = 288	$3.65 \cdot 10^{-5}$	7.4
nL = 576	$7.17 \cdot 10^{-6}$	5.1

[a] Where we prescribed the analytic solution outside the band.

<div align="center">

TABLE V

Error Measures on H for Different Values of nL(0) Taken over the Whole Domain on a Global Reduced Lat–Lon Grid ($nP = nL(0)/2$)[a]

</div>

		$E_r(H)$	$\dfrac{E_r(H)_{\frac{nL}{2}(0)}}{E_r(H)_{nL(0)}}$
nL(0) = 72,	3 reductions resp. at $\phi = 60°, 70°, 80°$	$1.10 \cdot 10^{-2}$	
nL(0) = 144,	3 reductions resp. at $\phi = 60°, 75°, 82.5°$	$3.66 \cdot 10^{-3}$	3.0
nL(0) = 288,	4 reductions resp. at $\phi = 60°, 75°, 82.5°, 86.25°$	$3.40 \cdot 10^{-3}$	1.1
nL(0) = 576,	4 reductions resp. at $\phi = 60°, 75°, 82.5°, 86.25°$	$1.74 \cdot 10^{-3}$	2.0
nL(0) = 288,	3 reductions resp. at $\phi = 60°, 75°, 82.5°$	$1.77 \cdot 10^{-3}$	2.1
nL(0) = 576,	3 reductions resp. at $\phi = 60°, 75°, 82.5°$	$8.81 \cdot 10^{-4}$	2.0

[a] Where grid coarsening is performed at the given latitudes.

then be attributed to the fact that on finer grids the volumes move closer to the boundary of the band, where the one-dimensional character of our flow diminishes.

In case of a nonuniform grid we have no analytic order estimate. Therefore, to give an indication, a numerical order estimate is computed. We evaluate the results found after calculations on a global reduced lat–lon grid. We ran four tests, each time doubling the value of nL(0) defined as the amount of grid cells in the longitudinal direction on the unreduced grid part. We begin with nL(0) = 72. The cell distribution in the unreduced grid part is uniform. We again coarsen our grid each time the cell width in the longitudinal direction projected onto the sphere is reduced by a factor 2 compared to the preceding reduction. In case of our grids, this rule yields three or four reductions. To make sure that our grid is not too coarse in regions close to the poles, we also ran test on grids with nL(0) = 288 and nL(0) = 576 where three instead of four reductions were applied as was originally prescribed by the reduction rule. The error measures on H, $E_r(H)$, are shown in Table V. This time the max-norm is taken over the whole domain. The entries in the third column yield the order factor. Per grid we give the amount of reductions and their corresponding latitudes.

First, the results show that the reduced grid approach leads to first-order accuracy. It should be noted though, that the error estimate is calculated in the max-norm over the whole domain. At the interface between the reduced grid parts we suffer from order reduction. Along the rest of our domain nearly second-order accuracy is found. Again, the grid must not be too coarse in the polar area. In case of nL(0) = 288 with four reductions, this condition is obviously not fulfilled, resulting in almost no error reduction. Compared to unreduced grids—see, for instance, the entry 9.82×10^{-3} from Table II and 1.09×10^{-2} in Table V— the reduced grid approach results in a small accuracy loss on coarse grids. The accuracy loss on finer grids will be larger since we find first-order accuracy on a reduced lat–lon grid. However, its positive influence on the stability restriction for explicit time stepping compromises its use. As long as we take special care to guarantee an acceptable amount of grid cells next to the poles, the errors are sufficiently small for practical purposes.

We here omit an order estimate for calculations on a combined grid. As we will later show, the results mimic the accuracy behavior found on the reduced lat–lon grids. Investigations related to the connection problem are reported in the next section.

4.1.2. *Placement of the Stereocap*

As nicely illustrated by Fig. 9, in stereographic coordinates velocities over the poles behave normal and smoothly and hence can be approximated with much greater accuracy
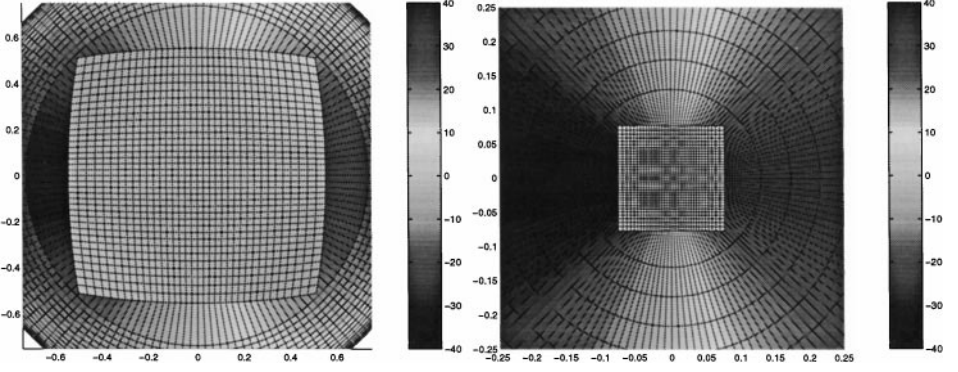
FIG. 11. Projection of two combined grids (nL = 144) onto the cartesian (x, y) plane $(z = 0)$, where the stereocap in the right picture is moved closer to the pole. $\bar{\phi} = 47.5°$ (left) and $\bar{\phi} = 87.5°$ (right). Along the axes, the x and y coordinates are given as multiples of the earth radius.

using a stereocap. However, we have also concluded that to cover the whole sphere a stereographic grid must be combined with, for instance, a lat–lon grid, creating a connection problem as examined in Section 3. In addition to the question of how this connection problem influences the accuracy, we wish to answer the question of what value we should take for $\bar{\phi}$, which we defined in Section 3.1 as the latitudinal boundary of the uniform lat–lon region R_{II}. We expect these questions to be related, since the larger $\bar{\phi}$, the smaller the cells in the connection band. We ran four tests on a combined unreduced grid, having nL = 144 points, i.e., with $\Delta\lambda = \Delta\phi = 2.5°$, where we gradually changed $\bar{\phi}$. Figure 11 shows the combined grids in case of the extreme values of $\bar{\phi}$. We coupled x_r defined in Section 3.1 as the x_{st} coordinate of the top right-hand corner of the stereocap to $\bar{\phi}$, following $\phi_{x_r} = \bar{\phi} + \Delta\phi/2$. ϕ_{x_r} denotes the latitude corresponding to the stereographic coordinates $(x_{\mathrm{st}}, y_{\mathrm{st}}) = (x_r, y_r)$. Table VI displays the different error measures on H, u and U over five different regions, i.e.,

TABLE VI

Error Measures on H, u, and U for Different Values of $\bar{\phi}$ on Four Combined Uniform Lat–Lon Stereographic Grids (nL = 144)

	$E_r(H)_{\text{lat–lon grid part}}$	$E_r(H)_{\text{equator}}$	$E_r(H)_{\text{interface}}$	$E_r(H)_{\text{stereo grid part}}$	$E_r(H)_{\text{pole}}$
$\bar{\phi} = 47.5°$	$1.40 \cdot 10^{-1}$	$1.35 \cdot 10^{-1}$	$4.56 \cdot 10^{-2}$	$5.10 \cdot 10^{-2}$	$3.86 \cdot 10^{-2}$
$\bar{\phi} = 57.5°$	$7.58 \cdot 10^{-2}$	$3.64 \cdot 10^{-2}$	$3.27 \cdot 10^{-2}$	$1.41 \cdot 10^{-2}$	$7.14 \cdot 10^{-3}$
$\bar{\phi} = 67.5°$	$2.15 \cdot 10^{-2}$	$1.90 \cdot 10^{-2}$	$1.14 \cdot 10^{-2}$	$6.57 \cdot 10^{-3}$	$2.94 \cdot 10^{-3}$
$\bar{\phi} = 77.5°$	$2.48 \cdot 10^{-3}$	$2.30 \cdot 10^{-3}$	$2.31 \cdot 10^{-3}$	$7.42 \cdot 10^{-4}$	$3.00 \cdot 10^{-4}$
$\bar{\phi} = 87.5°$	$1.29 \cdot 10^{-3}$	$1.29 \cdot 10^{-3}$	$6.67 \cdot 10^{-4}$	$6.33 \cdot 10^{-4}$	$6.00 \cdot 10^{-4}$
	$E_a(u)_{\text{lat–lon grid part}}$	$E_a(u)_{\text{equator}}$	$E_a(u)_{\text{interface}}$	$E_a(U)_{\text{stereo grid part}}$	$E_a(U)_{\text{pole}}$
$\bar{\phi} = 47.5°$	43.06	17.45	43.06	37.38	$6.0 \cdot 10^{-2}$
$\bar{\phi} = 57.5°$	21.31	11.00	21.31	19.19	$3.6 \cdot 10^{-2}$
$\bar{\phi} = 67.5°$	5.23	2.39	5.23	3.43	$1.3 \cdot 10^{-2}$
$\bar{\phi} = 77.5°$	0.84	0.27	0.84	0.58	$3.8 \cdot 10^{-4}$
$\bar{\phi} = 87.5°$	0.14	0.02	0.14	0.30	$2.8 \cdot 10^{-4}$

Note. We give the errors $E_r(H)$, $E_a(u)$, and $E_a(U)$ over five different regions, i.e., over the uniform lat–lon grid part, over the cells located at the equator, over the interface cells connecting the two grids, over the stereographic grid parts, and over the cells next to the poles.

over the uniform lat–lon grid part, over the cells located at the equator, over the interface cells connecting the two grids, over the stereographic grid parts, and over the cells next to the poles. Note that the interface cells, the cells located at the equator, and the cells next to the poles are also included in the lat–lon grid part or the stereographic parts; see Section 3.1. $E_r(H)$ again describes the max-norm of the relative error on H. $E_a(u)$ and $E_a(U)$ describe max-norms of the absolute error on u and U, respectively.

As expected, Table VI shows that it is best to make the stereocap as small as possible, restricting accuracy loss due to the connection problem at the grid interface. The influence of reducing the size of the interface cells is particularly visible when concentrating on the maximum absolute error of the velocities. We encounter an unavoidable accuracy reduction at the grid interface. However, on grids with a small size stereocap this error is sufficiently small. Furthermore, both errors on H and U are impressively small at the poles. Comparing the overall error $E_r(H)$ for $\bar{\phi} = 77.5°$ with the second entry from Table V, we see that our calculations on a combined grid with a stereocap result in the same overall accuracy as the calculations on a compatible reduced grid. Note that this conclusion is true for modest and small sized stereocaps. For large stereocaps the interface cells become too distorted.

4.1.3. A Combined Grid with Realistic Refinement

Figure 11 shows that our conclusion should be handled with some consideration. When performance issues are important, the resolution increase on the stereocap due to size reduction can lead to a cut-back on the time-step caused by stability restrictions. However, this problem is easily resolved when we add the reduced grid approach to our combined grid. To show this, we end our numerical section on test case 2 of [27] by giving the results of a test on a combined reduced grid with realistic refinements. The stereocap is placed such that $\bar{\phi} = 85.625°$, $nL(0) = 576$, and $nP = 288$. We apply three reductions, one at $60°$, one at $75°$, and one at $82.5°$.

The results confirm our expectations. We find a maximum relative error on H over our whole domain of $E_r(H) = 8.6 \times 10^{-4}$ and a maximum absolute error on u, U of $E_a(u, U) = 0.092$. These errors show that a combined grid provides a good alternative to a global reduced lat–lon grid; see Table V case $nL(0) = 576$ with three reductions. This conclusion holds in particular when the CFL restriction demands a too coarse lat–lon grid around the poles to maintain an acceptable time-step. This follows in comparing the smallest grid sizes found on the two different grid types. Note that in either case the smallest step size is found next to the poles. For the combined grid, the smallest grid size on the globe approximately reads

$$\frac{\sqrt{2}\pi a \cos\bar{\phi}}{nL_{interface}}. \tag{4.6}$$

On a reduced lat–lon grid, the smallest grid size reads

$$\frac{2\pi a \cos(90° - \Delta\phi)}{nL_{interface}}. \tag{4.7}$$

Based on (4.6) and (4.7), we give the smallest grid size ratio for $\Delta\phi = 0.625°$, $nL_{interface} = 72$

and $\bar{\phi} = 85.625°$. The ratio reads

$$\frac{\frac{1}{2}\sqrt{2}\cos\bar{\phi}}{\cos(90° - \Delta\phi)} \approx 4.95.$$

For explicit integration methods this ratio suggests a difference in computing time of approximately a factor of 5 in favor of the combined grid. Note that the time step restriction can indeed be encountered in practical situations, since high-velocity components do occur in the polar areas.

5. CONCLUDING REMARKS

Spectral methods currently dominate the field of approximation methods used in global circulation modeling. Since spectral methods become relatively expensive on fine grids, the demand for higher grid resolution and the better prospects for parallelization and local grid refinement have renewed interest in gridpoint methods. In this paper we have studied a sophisticated finite volume scheme for the spatial discretization of the SWEs in spherical geometry, viz., Osher's scheme [15] using the P-variant of Hemker and Spekreijse [8] for the integration path in the flux evaluation and third-order upwinding for the determination of the constant states. The scheme's second-order accuracy, its robustness and its apprehension for the characteristic directions associated with the nonlinear equations, makes it a possible competitor to spectral methods for computations on fine grids. Note that in case of a combined grid, our method is second-order accurate in smooth regions away from the grid interface and first-order otherwise.

We have paid special attention to the pole singularity and the associated CFL restriction. We have examined a combined grid to thoroughly alleviate the associated problems. This combined grid connects a stereographic grid in the polar regions with a lat–lon grid used at low latitudes. We have found that it is best to keep the size of the stereocap rather small to minimize connection errors at the grid interface. Since a small stereocap involves small grid sizes at and near the cap, grid reduction in the lat–lon part can be used when it is needed to avoid very small grid sizes. In this manner the time step limitation for explicit integration methods emanating from the pole problem can be significantly reduced. Therefore, the resulting combined grid is advocated to be used together with an explicit integration scheme. In case time step stability plays a minor role, or when an implicit type integration method is used, we advocate using only a lat–lon grid, possibly reduced, because this approach is simpler. However, on lat–lon grids the singularity remains so that in case of flow over the poles the grid should be sufficiently fine.

Our findings are based on test cases 1, 2, and 6 of the standard test set from [27]. To save space we have shown results for test case 2 only. In the near future we will present results on time integration aspects using the spatial discretizations described in the current paper.

REFERENCES

1. J. G. Blom, W. Hundsdorfer, and J. G. Verwer, *Vectorization Aspects of a Spherical Advection Scheme on a Reduced Grid*, Technical Report NM-R9418, CWI, Amsterdam, 1994.

2. G. L. Browning, J. J. Hack, and P. N. Swarztrauber, A comparison of three numerical methods for solving differential equations on the sphere, *Mon. Wea. Rev.* **117**, 1058 (1989).

3. K. Cassirer, R. Hess, C. Jablonowski, and W. Joppich, *The Shallow Water Test Cases for a Global Model with Documentation of the Results*, Arbeitspapiere der GMD 999, GMD, 1996.

4. T. Davies and J. C. R. Hunt, New developments in numerical weather prediction, in *Numerical Methods for Fluid Dynamics V*, edited by K. W. Morton and M. J. Baines (Clarendon Press, Oxford, 1995).

5. ECMWF, ECMWF Forecast Model Documentation, European Centre for Medium-Range Weather Forecasts, Shinefield Park, England, ECMWF Research Manual edition, 1988.

6. E. B. Eliasen, B. Machenhauer, and E. Rasmussen, *On a Numerical Method for Integration of The Hydrodynamical Equations with a Spectral Representation of the Horizontal Fields*, Report No. 2, Institut for Teoretisk Meteorologi, University of Copenhagen, 1970.

7. G. J. Haltiner and R. T. Williams, *Numerical Prediction and Dynamic Meteorology* (Wiley, 2nd ed., 1980).

8. P. W. Hemker and S. P. Spekreijse, Multiple grid and Osher's scheme for the efficient solution of the steady state Euler equations, *Appl. Numer. Math.* **2**, 475 (1986).

9. C. Hirsch, Numerical Computation of Internal and External Flows, Vol. 2, *Computational Methods for Inviscid and Viscous Flow* (Wiley, Chichester, 1990).

10. J. R. Holton, An Introduction to Dynamic Meteorology (Academic Press, San Diego, 1992).

11. D. Lanser, J. G. Blom, and J. G. Verwer, *Spatial Discretization of the Shallow Water Equations in Spherical Geometry Using Osher's Scheme*, Technical Report MAS-R9918, CWI, Amsterdam, 1999.

12. J. L. Lions, R. Temam, and S. Wang, New formulations of the primitive equations of atmosphere and applications, *Nonlinearity* **5**, 237 (1992).

13. S. A. Orszag, Transform method for calculation of vector coupled sums: Application to the spectral form of the vorticity equation, *J. Atmos. Sci.* **27**, 890 (1970).

14. S. Osher and S. Chakravarthy, Upwind schemes and boundary conditions with applications to Euler equations in general geometries, *J. Comput. Phys.* **50**, 447 (1983).

15. S. Osher and F. Solomon, Upwind difference schemes for hyperbolic systems of conservation laws, *Math. Comp.* **38**, 339 (1982).

16. N. A. Phillips, A map projection system suitable for large-scale numerical weather prediction, *J. Meteor. Soc. Japan* **75**, 262 (1957).

17. C. Ronchi, R. Iacono, and P. S. Paolucci, The cubed sphere: A new method for the solution of partial differential equations in spherical geometry, *J. Comput. Phys.* **124**, 93 (1996).

18. R. Sadourny, Conservative finite-difference approximations of the primitive equations on quasi-uniform spherical grids, *Mon. Wea. Rev.* **100**, 136 (1972).

19. S. P. Spekreijse, *Multigrid Solution of the Steady Euler Equations*, Number 46 in CWI Tracts (CWI, Amsterdam, 1988).

20. B. Spotz, M. Taylor, and P. Swarztrauber, *Shallow Water Equations on the Sphere*, http://www.scd.ucar.edu/css/staff/spotz/research/swell.html#STM.

21. G. Starius, Composite mesh difference methods for elliptic and boundary value problems, *Numer. Math.* **28**, 243 (1977).

22. J. J. Stoker and E. Isaacson, Final report 1. Technical Report IMM 407, Courant Institute of Mathematical Sciences, New York University, 1975.

23. B. van Leer, Towards the ultimate conservative difference scheme. III. Upstream-centered finite-difference schemes for ideal compressible flow, *J. Comput. Phys.* **23**, 276 (1977).

24. D. L. Williamson, Integration of the barotropic vorticity equation on a spherical geodesic grid, *Tellus* **20**, 642 (1968).

25. D. L. Williamson, Review of numerical approaches for modeling global transport, in *Air Pollution Modeling and Its Application IX*, edited by H. van Dop and G. Kallos, Nato Challenges of Modern Society, Plenum Press, New York, 1992, p. 377.

26. D. L. Williamson and G. L. Browning, Comparison of grids and difference approximations for numerical weather prediction over a sphere, *J. Appl. Meteor.* **12**, 264 (1973).

27. D. L. Williamson, J. B. Drake, J. J. Hack, R. Jacob, and P. N. Swarztrauber, A standard test set for numerical approximations to the shallow water equations in spherical geometry, *J. Comp. Phys.* **102**, 211 (1992).